

Solar-pumped Radiation-balanced Laser

Michael Küblböck,^{1,2,3} Mohammad Sahil,^{1,2} and Hanieh Fattahi^{1,2, a)}

¹⁾*Max Planck Institute for the Science of Light, Staudstrasse 2, Erlangen, 91058, Germany*

²⁾*Friedrich-Alexander-Universität Erlangen-Nürnberg, Staudstrasse 7, Erlangen, 91058, Germany*

³⁾*Graduate School in Advanced Optical Technologies (SAOT), Konrad-Zuse-Straße 3, Erlangen, 91052, Germany*

Solar-pumped lasers, predominantly based on neodymium gain media, offer a promising route to renewable laser–energy conversion and space-based photonics; however, their performance has been constrained by thermal loading and limited power scalability. Here, we propose and numerically investigate a solar-pumped ytterbium thin-disk gain medium in combination with a dome concentrator that enables multipass solar pumping and enhanced absorption. The design yields comparably low lasing thresholds for neodymium- and ytterbium-doped media, while ytterbium provides superior power scalability, enabling up to threefold higher output power. We further identify ytterbium-doped medium combined with a spherical concentrator as a viable solar-pumped, radiation-balanced configuration, achieving self-cooled lasing at solar pump intensities of 28.5 kW cm^{-2} within the 1020–1033 nm window of the solar spectrum. The spherical concentrator increases the averaged fluence of the solar pump while permitting anti-Stokes fluorescence to escape efficiently. These results establish multi-pass, solar-pumped thin-disk ytterbium lasers as a compact, scalable, and sustainable platform for high-performance solar-pumped lasers.

^{a)}Electronic mail: hanieh.fattahi@mpl.mpg.de

INTRODUCTION

Solar-pumped lasers have gained significant attention over the past decade as a sustainable technology with potential applications in renewable energy, green laser systems, communications, and space exploration, particularly for future lunar infrastructure^{1–8}. Most demonstrated systems employ solid-state rod lasers that harness the sun’s abundant energy and convert it directly into tens of watts of coherent optical power. However, their overall efficiency remains constrained by the substantial thermal load imposed on the gain medium.

The first continuous-wave solid-state solar laser, demonstrated by Young, utilized a neodymium-doped yttrium aluminum garnet (Nd:YAG) crystal as the gain medium⁹. Nd³⁺, a well-known four-level laser ion, offers a low lasing threshold and broad absorption bands spanning the visible to near-infrared spectrum^{10–12}. Its emission cross-section bandwidth of approximately 0.6 nm enables the generation of nanosecond-scale pulses. In Nd:YAG systems, however, the Nd³⁺ doping concentration is typically limited to approximately 1.1% due to fluorescence quenching, which reduces the fluorescence lifetime at higher dopant levels. This behavior is intrinsic to Nd³⁺ and arises from cross-relaxation within the $4F_{3/2}$ manifold as well as near-field electric-dipole interactions between adjacent Nd³⁺ ions under continuous pumping^{13,14}. At lower doping levels, a longer optical path within the gain medium is required to ensure sufficient pump absorption. As operating power increases, thermal management becomes a critical design constraint. Excess heat generated by quantum defects and non-radiative decay processes produces temperature gradients within the crystal, leading to transient thermal lensing and beam distortion. These effects exacerbate non-radiative losses and induce depolarization^{15–19}. Although numerous strategies have been investigated to improve the performance of solar-pumped lasers and mitigate thermal load^{1,12,20,21}, effective thermal management remains a persistent and central challenge.

Ytterbium (Yb)-doped YAG provides markedly superior thermal performance compared to Nd:YAG, primarily due to its lower quantum defect. As a quasi-three-level gain medium, Yb:YAG features a broad emission bandwidth that enables pulse durations down to a few hundred femtoseconds. Near room temperature, its emission and absorption spectra partially overlap, and the material exhibits reduced optical quenching, allowing doping concentrations beyond 10%²². However, the small energy gap between the lower laser level ($^4I_{13/2}$) and the ground state leads to significant thermal population, increasing the lasing threshold relative

to Nd-based systems and requiring higher pump intensities. Despite this higher threshold, Yb:YAG has become the dominant gain medium for high-peak-power laser development over the past several decades, owing to its long upper-state lifetime and excellent optical properties²³. In Yb:YAG, the thermal population of the terminal laser level further reduces efficiency, intensifying thermal management challenges and causing thermo-optic distortions. To mitigate these effects and improve beam quality, Yb³⁺lasers have been realized in a variety of geometries, including fiber, thin-disk, and slab configurations²³⁻³³.

In Yb:YAG thin-disk lasers, the active medium is water-cooled through one of its flat faces. The high surface-to-volume ratio enables efficient heat removal into the heat sink, resulting in a nearly uniform transverse temperature gradient within the homogeneously pumped central region of the disk. This minimizes stress-induced birefringence, thermal lensing, and aspherical aberrations, thereby preserving diffraction-limited beam quality. The cooled crystal face is often coated to function as a folding mirror or the end mirror of the resonator. To overcome the reduced pump absorption inherent to the thin gain medium, a multi-pass pumping scheme is employed in which multiple parabolic mirrors redirect pump light through the medium several times. The arrangement of parabolic mirrors determines the number of passes, which in turn directly affects both pump absorption efficiency and the resulting beam quality³⁴.

Moreover, Yb³⁺ ions are well suited for radiation-balanced lasing, as they possess only one excited manifold and exhibit no excited-state absorption, avoiding heat generation from multi-phonon decay³⁵. In radiation-balanced lasers (RBL), the pump wavelength is red-shifted relative to the mean fluorescence wavelength of the gain medium, enabling anti-Stokes fluorescence cooling³⁶. In this process, energy in the form of phonons is transferred from the host material to the emitting ions, maintaining thermal equilibrium and cooling the gain medium. Under RBL conditions, the spontaneous fluorescence rate is comparable to the stimulated emission rate. This enables heat and entropy produced by optical pumping, due to quantum defects and other nonradiative processes, to be dissipated via anti-Stokes fluorescence, reducing excess heat below the quantum defect limit³⁷⁻⁴⁰.

Radiation cooling has been demonstrated in Yb:YAG slab lasers⁴¹⁻⁴³ and thin-disk lasers⁴⁴⁻⁴⁶ by pumping the gain medium with a narrowband laser under RBL conditions⁴⁷. Recent studies further suggest that optical cooling can also be achieved using incoherent illumination, such as light-emitting diodes or spectrally filtered sunlight, with efficiencies

comparable to those obtained with coherent, laser-based pumping⁴⁸.

In this work, we investigate the feasibility of implementing thin-disk geometries for solar-pumped laser operation, with particular emphasis on determining whether radiation-balanced lasing (RBL) can be achieved to support sustainable, self-cooling performance. We first analyze an advanced solar-pumped thin-disk architecture employing Yb³⁺ as the gain medium. This design incorporates a water-cooled thin disk gain medium in combination with a solar-concentrating dome that traps and re-images the incident sunlight, thereby significantly enhancing the effective pump fluence on the gain medium. The concentrator geometry is optimized to address challenges associated with the low spatial coherence of solar radiation, which typically limits the utility of conventional multi-pass pumping approaches. Our results demonstrate that this concept can operate under direct solar pumping and can outperform traditional solar-pumped Nd³⁺-doped gain media.

Building on these insights, we then examine a solar-pumped, radiation-balanced Yb:YAG laser. In particular, we evaluate the impact of pump spectral bandwidth on both laser gain and radiative cooling, and we identify the boundary conditions necessary to sustain RBL operation. We further introduce a spherical concentrator to increase the solar pump fluence on the gain medium. The proposed scheme enables efficient extraction of anti-Stokes fluorescence and supports RBL operation in both thin-disk and rod geometries utilizing Yb:YAG as the gain medium. These studies outline promising directions for the development of thermally resilient, energy-efficient, and environmentally sustainable solar-pumped laser technologies.

WATER-COOLED SOLAR-PUMPED THIN-DISK LASER

A systematic investigation of both Yb³⁺ and Nd³⁺ gain media was conducted to evaluate the feasibility of implementing a thin-disk geometry (see Methods). For scalability and consistent comparison, we assumed that 1 m² of sunlight is collected and concentrated onto the gain medium. The incident solar spectrum for optical pumping was selected to match the specific absorption characteristics of each material. Owing to the broad absorption bandwidth of Nd³⁺, the unfiltered extraterrestrial solar spectrum spanning from 200 nm to 3000 nm, corresponding to a total irradiance of 1367 W m⁻², was employed to pump the Nd:YAG thin-disk medium. The resonator configuration for this system was designed to

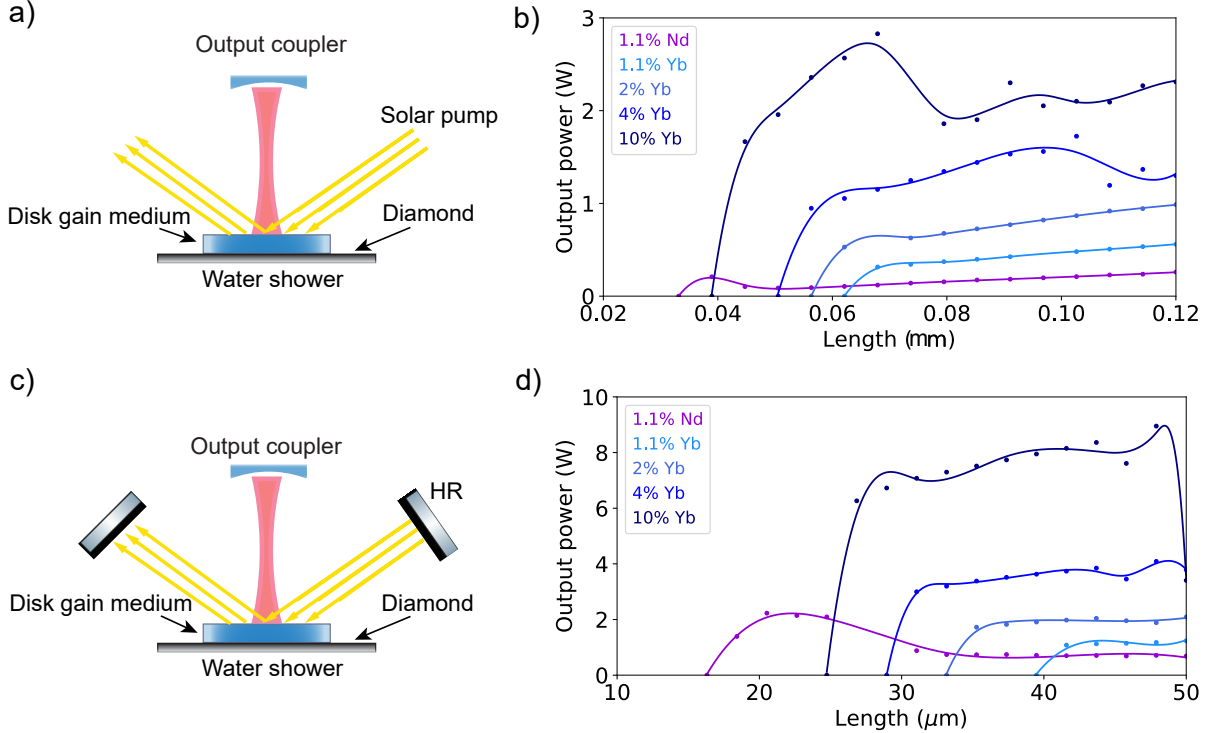


FIG. 1: **Comparison of Nd^{3+} and Yb^{3+} gain media in a thin-disk geometry.** a) Schematic of a single-pass solar-pumped thin-disk laser. b) The output power versus gain medium thickness of the single-pass pumped laser cavity for a 1.1 % -doped Nd:YAG and various doping concentrations from 1.1 % to 10 % for Yb:YAG thin-disk. c) Schematic of a six-pass solar-pumped thin-disk laser. d) The output power versus thickness of a six-pass solar-pumped laser with a 1.1 % -doped Nd:YAG and various doping concentrations from 1.1 % to 10 % for Yb:YAG. The unfiltered solar irradiance of 1367 W m^{-2} for Nd:YAG and the filtered solar irradiance of 85.8 W m^{-2} for Yb:YAG are considered for both schemes.

support lasing at 1064 nm. In contrast, pumping of the Yb:YAG gain medium utilized a spectrally filtered portion of the extraterrestrial solar spectrum restricted from 890 nm to 990 nm, for which the available solar irradiance is 85.8 W m^{-2} . The laser cavity for the Yb:YAG system was correspondingly optimized to achieve emission at 1030 nm.

The thin-disk gain medium was mounted on a diamond substrate that was cooled from below using a water shower, while the top and lateral surfaces of the disk remained uncooled and exposed to ambient air. The front surface of the gain medium was coated with a 100 % anti-reflection layer, whereas the rear surface of the gain medium and the diamond

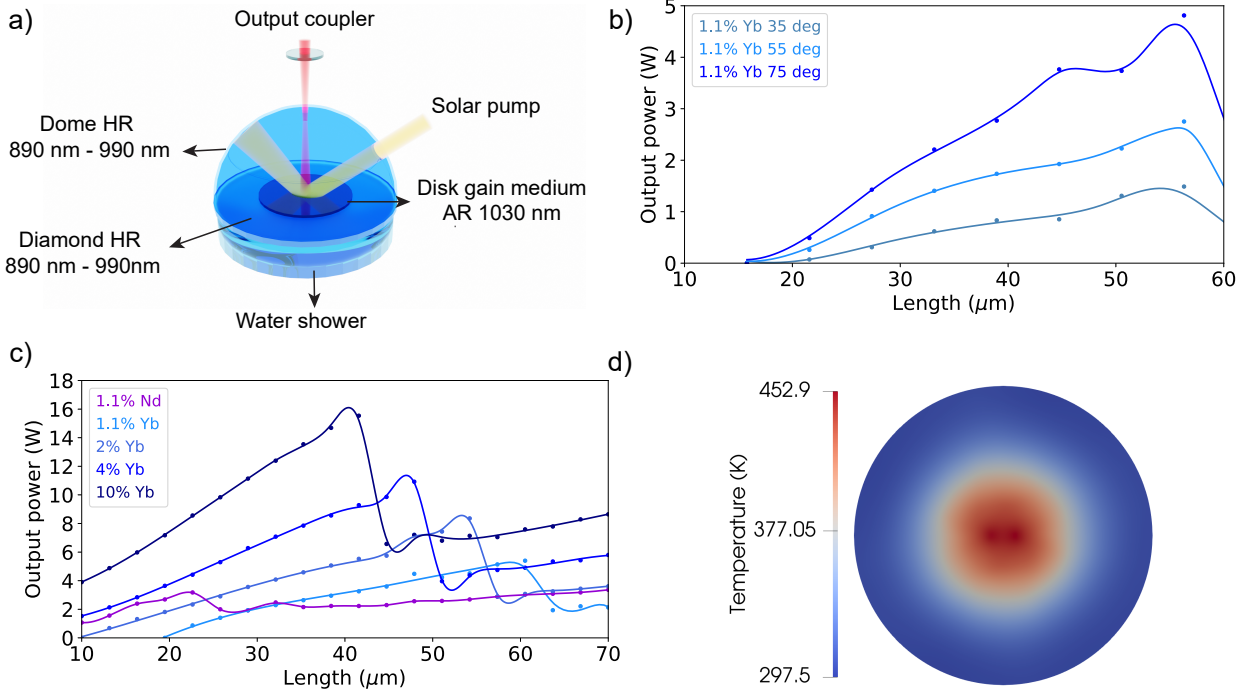


FIG. 2: Dome solar-pumped thin-disk laser. a) Schematic of a dome solar-pumped thin-disk laser. b) The thickness of the crystal versus the output power of the laser for various solar incident angles. The calculation is performed for 1.1%-doped Yb:YAG gain medium. c) The output power of the dome concentrator concept versus the thickness of the gain medium. It is assumed that the solar beam enters the dome at an oblique angle of 75°. d) Temperature distribution on the thin-disk for a 10% Yb-doped gain medium at a thickness of 40 μm and solar pump incident angle of 75°.

surface were coated with a 99.5 % reflective layer at both the pump and lasing wavelengths. Pumping was implemented in a quasi-end-pumped configuration, where the incident pump beam traverses the crystal at an oblique angle. To assess the degree of saturation in the gain medium and quantify the influence of the proposed integrated dome, we first examined the laser output power as a function of the number of controlled passes of solar light through the gain medium. Fig. 1a depicts the cavity geometry corresponding to the single-pass solar-pumping configuration.

For Nd:YAG, a doping concentration of 1.1 % was assumed, as this value is considered optimal due to the larger ionic radius of Nd^{3+} compared with Y^{3+} . Higher Nd^{3+} doping levels introduce significant lattice stress during crystal growth, which often leads to dislocations and other material defects⁴⁹. A fluorescence lifetime of 235 μs was used for the Nd:YAG

simulations. Yb:YAG can accommodate Yb^{3+} doping levels up to approximately 25 %, owing to the close similarity in ionic radii between Yb^{3+} and Y^{3+} ^{50,51}. However, the doping concentration was varied only from 1.1 % to 10 %, as higher concentrations are known to induce concentration quenching^{22,41–43,52}. A constant fluorescence lifetime of 1 ms was assumed over this doping range. Fig. 1b presents the resulting output power for single-pass pumping at various gain-media thicknesses and doping concentrations. It is observed that Nd:YAG exhibits a lower lasing threshold than Yb:YAG at comparable doping levels, primarily due to its four-level energy level scheme. Yb:YAG requires roughly an order of magnitude higher doping to achieve a similar threshold. However, it provides up to three times greater output power.

A second series of simulations was performed to investigate the effect of re-imaging the residual reflected pump power for up to five additional passes, thereby enabling multi-pass pumping to compensate for the inherently low single-pass gain in the thin-disk geometry. Fig. 1c illustrates the schematic of the six-pass pumping configuration, and Fig. 1d presents the corresponding output-power scaling. The results show up to a twofold reduction in the lasing threshold across the range of doping concentrations and gain-medium thicknesses examined.

Because the solar beam is only partially coherent with a short coherence length^{53,54}, efficiently re-imaging it with conventional mirror arrangements presents a significant challenge. To address this limitation, we developed a re-imaging concept tailored for solar-pumped thin-disk lasers (Fig. 2a). The design incorporates a spherical half-dome with a diameter of 25 mm, which serves to confine and redirect the solar radiation, enabling effective multi-pass pumping. For the simulations, a round emitter of 2 mm diameter was defined on the dome surface. The inner surface of the dome was assumed to be coated with a 100 % reflective layer at the pump wavelength, except in the emitter region. Rays impinging on the emitter were considered fully absorbed, reproducing the function of a 2 mm entrance aperture through which the solar beam enters the dome.

Since only a small fraction of the pump radiation is absorbed in each pass, multi-pass operation is achieved by allowing the pump beam, after transmission through the gain medium, to reflect from its rear surface back toward the inner surface of the dome. This process continues iteratively until the beam is eventually redirected onto the emitter aperture and exits the dome. This geometry, therefore, enables multiple effective pump passes while accommo-

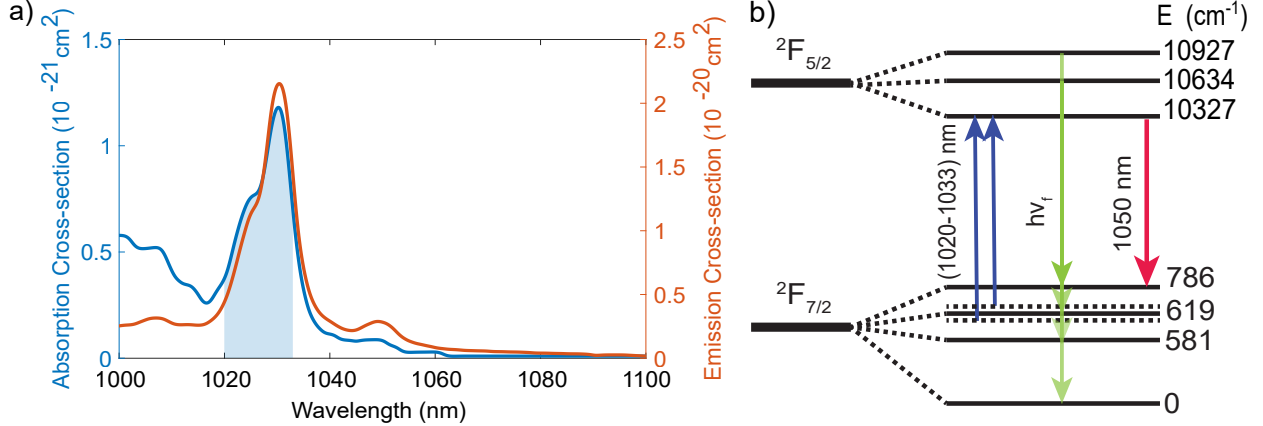


FIG. 3: Required properties of Yb^{3+} ions for radiation balanced lasing. a) Absorption and emission cross section of Yb^{3+} . The blue shaded area shows the filtered spectral bandwidth in the solar spectrum from 1020 nm to 1033 nm to pump the Yb:YAG gain medium for radiation-balanced operation. b) Energy level diagram of the Yb:YAG gain medium in the radiation balance regime. The blue arrows show the pump spectrum, the red arrow is the lasing wavelength, and the green arrows (ν_f) refer to the anti-Stokes emission.

dating the limited spatial coherence of solar radiation. Fig. 2b illustrates the dependence of the laser output on the incident angle of the solar pump beam on the gain medium. The results indicate that smaller incident angles, i.e., those closer to normal incidence on the thin disk, produce higher output power. This improvement can be attributed to the enhanced spatial overlap between the pumped volume in the gain medium and the laser cavity mode.

As shown in Fig. 2c, implementing the dome-based multi-pass pumping scheme lowers the lasing threshold for both gain media substantially compared to the other geometries. In addition, saturation is achieved at smaller gain-medium thicknesses for lower Yb:YAG doping concentrations, indicating more efficient pump utilization and improved cooling within the thin-disk configuration. The highest output power is obtained for a Yb:YAG gain medium with 10% doping and a thickness of 40 μm . Beyond this regime, the thermal load on the gain medium leads to surface deformation, thermal lensing, and mechanical stress within the crystal. Fig. 2d illustrates the resulting thermal distribution and surface deformation along the x-axis of the disk beyond 40 μm thickness.

RADIATION-BALANCED SOLAR-PUMPED THIN-DISK LASER

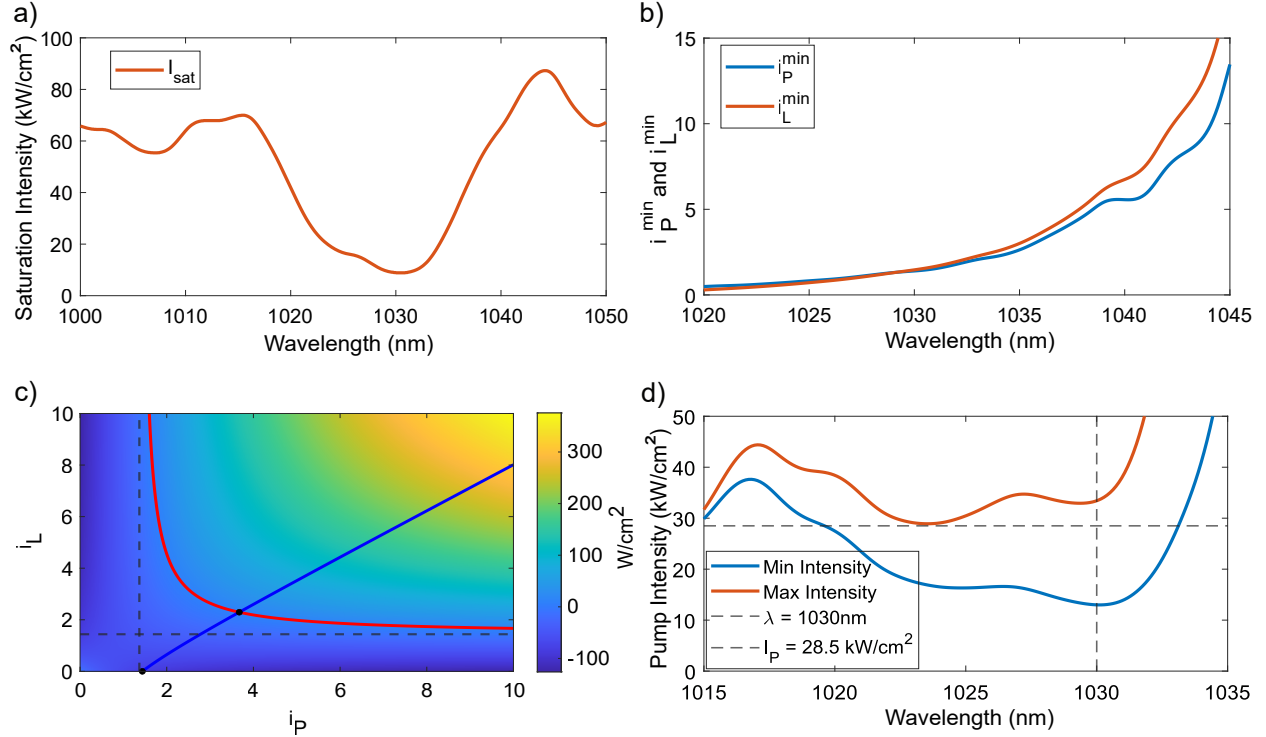


FIG. 4: Required solar spectrum and solar intensity for radiation balanced lasing. a) Wavelength-dependent required intensity to saturate the atomic transition in Yb:YAG gain medium. b) The minimum pump (i_P^{min}) and lasing (i_L^{min}) intensities required to achieve RBL for various pump wavelengths. c) Thermal power density map for pump wavelength $\lambda_P = 1030\text{ nm}$ and lasing wavelength $\lambda_L = 1050\text{ nm}$. The Red curve represents the exact condition for RBL, and the blue curve illustrates the relationship between normalized pumping and lasing intensities. For this simulation, the crystal length of 1 mm with a doping concentration of 5%³⁶ and cavity loss of 0.5% is assumed. d) RBL range is defined for solar spectral bandwidth of 1020 nm to 1033 nm. The blue curve indicates the threshold pump intensity. The orange curve shows the maximum allowed pump intensity for operation in RBL.

During laser operation, optical pumping at photon energy $h\nu_P$ establishes a population inversion, which subsequently leads to stimulated emission at the lower photon energy $h\nu_L$. The net thermal load in the gain medium arises from the difference between the absorbed pump power and the total emitted optical power. The latter includes both stimulated

emission (laser output) and spontaneous emission (fluorescence) at frequency ν_f . In conventional lasers, anti-Stokes fluorescence is negligible because of its comparatively small emission cross section, resulting in a predominantly exothermic process where heat accumulates in the gain medium. However, when operating under the anti-Stokes-dominated condition $h\nu_L < h\nu_P < h\nu_f$, radiative processes can offset or even surpass the heat generated by nonradiative mechanisms, enabling athermal or radiation-balanced (self-cooling) laser operation (see Methods).

As previously noted, Yb:YAG possesses the requisite properties for operation as a cooling-grade gain medium, with a mean fluorescence wavelength of 1010 nm^{55,56}. Fig. 3a presents the absorption and emission cross sections of Yb:YAG within the spectral region relevant to radiation-balanced lasing near 1050 nm. To satisfy the anti-Stokes pumping condition, the pump wavelength must exceed the mean fluorescence wavelength, i.e., $\lambda_P > \lambda_f = 1010$ nm (see Fig. 3b). Both the absorption and emission cross sections exhibit significant wavelength-dependent variation across this region. Consequently, the required fractional excitation, as well as the minimum pump and laser intensities necessary for athermal operation, are strongly influenced by the choice of pump spectral bandwidth.

To determine an appropriate solar pumping spectrum capable of supporting radiation-balanced lasing in Yb:YAG, numerical simulations were performed. Fig. 4a illustrates the dependence of the saturation pump intensity on the spectral bandwidth of the solar irradiation considered suitable for radiation-balanced operation. At 1030 nm, where both the absorption and emission cross sections reach their maximum values, achieving transition saturation requires a pump saturation intensity of approximately 9 kW cm^{-2} within the gain medium (see eq. 6 in Methods).

Fig. 4b displays the wavelength dependence of the minimum pump and intra-cavity lasing intensities (see eq. 4 in Methods). Both values remain relatively close within the spectral range of 1020 nm to 1033 nm, but begin to diverge at longer wavelengths, indicating the need for higher intra-cavity laser intensity to meet the RBL condition. Figure 4c illustrates the relationship between pump intensity and intra-cavity laser intensity for a pump wavelength of 1030 nm. The red curve represents the condition of zero net heat deposition in the gain medium, defining the boundary for radiation-balanced operation. The blue curve shows the pump–laser intensity relationship under steady-state lasing.

Two key operating points appear as black markers on the blue curve. The lower marker

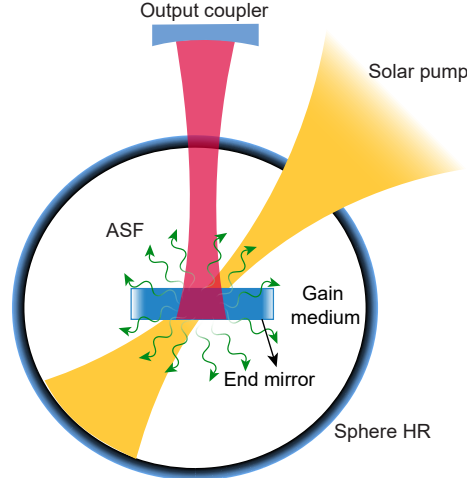


FIG. 5: Concept of a solar-pumped Yb:YAG laser including a sphere concentrator operating in the radiation-balanced regime. A spherical concentrator collects and refocuses sunlight onto the gain medium to increase pump fluence, while also enabling efficient extraction of anti-Stokes fluorescence (ASF) in all directions to support radiative cooling. The inner surface of the concentrator is coated for high reflectivity within the 1020 nm–1033 nm spectral band required for RBL operation, excluding the area for solar input.

indicates the lasing threshold at $i_P = 1.44$, corresponding to the minimum pump intensity required to sustain stimulated emission. The upper marker identifies the point at which the blue curve intersects the red curve, occurring at $i_P = 3.67$ and an intra-cavity intensity of $i_L = 2.29$. At this intersection, all heat generated in the crystal is fully compensated by anti-Stokes fluorescence, marking the onset of radiation-balanced lasing and establishing the maximum pump intensity that maintains cooling performance.

For stable radiation-balanced operation, the system must operate between these two limits. Below the lasing threshold, stimulated emission cannot be maintained. Above the radiation-balanced boundary, lasing may persist, but the net heat deposition becomes positive, resulting in heating of the gain medium. The accompanying colour map further illustrates the net heat deposition as a function of pump and intra-cavity laser intensities, distinguishing cooling-enabled conditions (below the red curve) from net-heating regions (above the red curve). Together, these results show that achieving simultaneous lasing and optical refrigeration in solar-pumping is feasible, but only within a constrained operational

window defined by both gain requirements and radiative cooling conditions.

These operational limits were evaluated for pump wavelengths longer than the mean fluorescence wavelength, while maintaining a fixed lasing wavelength of 1050 nm. Figure 4d summarizes the minimum and maximum pump intensities required for radiation-balanced operation when solar pumping is confined to the 1015 nm–1035 nm spectral range. The most favorable performance occurs between 1020 nm and 1033 nm, where the RBL condition is satisfied at a pump intensity of 28.5 kW cm^{-2} .

Within this wavelength range, the available solar power is approximately 9.5 W m^{-2} . When concentrated onto a 1 mm radius spot, this yields a peak intensity of only 302 W cm^{-2} . Achieving the required 28.5 kW cm^{-2} therefore necessitates either (i) increasing the solar collection area by more than two orders of magnitude or (ii) enhancing the pump fluence at the gain medium through multi-pass pumping. The former approach would demand excessively large and costly optics, making it impractical for compact laser systems. Consequently, multi-pass pumping represents a far more viable strategy for reaching the required intensities.

Fig. 5 illustrates a proposed configuration designed to enable RBL operation under multi-pass solar pumping. Because external thermal management is not required, a fully spherical concentrator geometry can be employed to efficiently re-image and confine sunlight onto the gain medium. Radiative heat extraction further allows the gain-medium thickness to be increased to achieve gain saturation without compromising thermal performance. The spherical geometry promotes isotropic escape of anti-Stokes fluorescence, thereby minimizing photon reabsorption and reducing the risk of radiative trapping. The gain medium may be implemented in either rod or thin-disk geometries. The inner surface of the concentrator is coated for high reflectivity within the solar pump bandwidth from 1020 nm to 1033 nm, while exhibiting anti-reflection at the laser wavelength of 1050 nm. One surface of the gain medium is coated to serve as the cavity end mirror with high reflectivity at 1050 nm, whereas the remaining surfaces are anti-reflection coated at the solar pump wavelengths to maximize pump coupling efficiency.

CONCLUSION

Solar-pumped lasers offer a compelling pathway toward renewable laser energy conversion and space-based photonic applications, yet their performance has long been constrained by thermal loading and limited power scalability, particularly in Nd:YAG systems. Although Nd:YAG exhibits favorable solar absorption and low lasing thresholds, its intrinsically limited doping concentration and associated thermal constraints fundamentally restrict achievable output power.

Here, we propose the concept of a solar-pumped thin-disk laser employing both Nd:YAG and Yb:YAG gain media. The thin-disk geometry enables efficient heat extraction, significantly suppressing thermal gradients and surface deformation; however, it suffers from low solar pump absorption per pass. We numerically demonstrate that while Nd:YAG benefits from a lower lasing threshold under single- and six-pass pumping compared to Yb:YAG due to its four-level energy scheme, this advantage becomes marginal when combined with the dome concentrator multi-pass pumping concept introduced in this work. The dome concentrator enhances solar photon trapping and absorption efficiency, enabling both gain media to reach comparably low lasing thresholds. Under these conditions, Yb:YAG clearly outperforms Nd:YAG, offering superior thermal management and markedly improved power scalability. The Nd:YAG doping limit of approximately 1.1%, imposed by fluorescence quenching, severely constrains output power. In contrast, thin-disk Yb:YAG supports substantially higher doping concentrations, up to 10%, enabling output powers up to three times higher than those achievable with Nd:YAG.

We further identified Yb:YAG as a strong candidate for a solar-pumped radiation-balanced laser (RBL), in which anti-Stokes fluorescence compensates for heat generated during lasing, enabling intrinsically self-cooled and fully sustainable operation. Our calculations show that RBL conditions can be reached at a solar pump intensity of approximately 28.5 kW cm^{-2} within a solar spectral window from 1020 nm to 1033 nm, suggesting that achieving full RBL operation under solar pumping requires a large collection area. However, the spherical multi-pass concentrator proposed here provides an effective solution by enhancing solar photon trapping while maintaining a compact system footprint. Radiative heat extraction further allows increased gain-medium thickness without compromising thermal performance, while the spherical geometry promotes isotropic escape of anti-Stokes flu-

rescence, minimizing photon reabsorption and radiative trapping. Both rod and thin-disk implementations are compatible with this concept.

These results establish Yb:YAG lasers combined with sphere-concentrator multi-pass solar pumping as a promising platform for compact, scalable, and high-efficiency solar-pumped laser systems. Future investigations may leverage Purcell-enhanced cavity designs to achieve additional reductions in radiation-balanced laser threshold requirements. This work lays the groundwork for sustainable photonic technologies with applications in space-based power generation, remote sensing, and advanced laser energy systems.

METHODS

Numerical simulations were performed using the “Advanced software for laser design”, which considers the superposition and competition of laser cavity modes via dynamic mode analysis^{57,58}. In dynamic mode analysis, rate equations are solved for each excited transverse mode in the cavity. The optical wave is then described as a dynamic superposition of several eigenmodes, allowing for the precise calculation of the laser output power and beam quality. The deformation of the gain medium, stress, and thermal effects are calculated via finite element analysis, and their impact on thermal lensing and the stability of the laser resonator is considered. Fig. 6 shows the absorption and emission cross sections and energy level diagram of Nd³⁺ and Yb³⁺ ions. The extraterrestrial solar spectrum from 200 nm to 3000 nm corresponding to 1367 W m⁻² solar irradiance was used to pump Nd:YAG gain medium, due to its broad absorption bandwidth. The laser cavity for Nd:YAG was designed for lasing at 1064 nm.

For pumping Yb:YAG gain medium, the filtered extraterrestrial solar spectrum with the bandwidth of 890 nm to 990 nm is used. The solar irradiance in this spectral bandwidth corresponds to 85.8 W m⁻². The laser cavity for Yb:YAG is designed for lasing at 1030 nm. It is assumed that the solar beam is focused to a 2 mm diameter by employing a primary and secondary collection^{59,60}. 500 000 rays were used to simulate the solar light via ray tracing. A disk-shaped gain medium with a diameter of 4 mm mounted on a 0.5 mm-thick diamond substrate with a 25 mm diameter is assumed for both gain media⁶¹. The diamond is cooled by a water shower from beneath. The top and the side surfaces of the gain medium are not cooled and are in ambient air under atmospheric pressure. The water cooling of the gain

medium is calculated via

$$k \cdot \frac{dT}{dn} - \beta \cdot (T - T_{\text{cool}}) \Big|_{\Gamma} = 0 \quad (1)$$

where β is the heat transfer coefficient. When cooling with a water shower, $0.05 \times 10^{-2} \text{ W mm}^{-1} \text{ K}^{-1}$ for β and 6 m s^{-1} for flow rate is assumed. We assumed a cooling temperature of 20°C and a thermal conductivity of $11 \text{ W m}^{-1} \text{ K}^{-1}$ for the YAG crystal.

It is assumed that the front surface of the gain medium and the diamond substrate have a 100 % anti-reflection coating, while the back surface of the gain medium has a 99.5 % reflective layer at the pump and lasing wavelengths. The gain medium is pumped in a quasi-end-pumped scheme, where the pump beam passes through the crystal under an oblique angle. The designed laser cavity for all the simulations in this section has a 25 mm length comprising a 99 % output coupler in a Fabry Pérot cavity. This cavity design corresponds to the mode diameter of 710 μm on the flat thin-disk gain medium (see Fig. 1a).

For RBL operation, the following formulation is considered. As derived in^{36,39,46}, during the lasing process, a pump laser with photon energy $h\nu_P$ creates population inversion, followed by stimulated emission at $h\nu_L < h\nu_P$. The net heat power deposited in the gain medium is the difference between the absorbed pump power and the emitted optical power. The latter is a combination of stimulated emission (laser) and spontaneous emission (fluorescence) at frequency ν_f :

$$H = \dot{n}_P h\nu_P - \dot{n}_L h\nu_L - \dot{n}_f h\nu_f. \quad (2)$$

Here, \dot{n}_P is the rate of photon absorption by the pump, \dot{n}_L is the stimulated emission rate, and \dot{n}_f is the spontaneous emission. Anti-Stokes fluorescence can be ignored for laser operation since $h\nu_P > h\nu_f$, as is the case in nearly all lasers. In this context, $H > 0$ represents an exothermic process, where heat is generated in the laser medium. In the anti-Stokes dominant condition given by $h\nu_L < h\nu_P < h\nu_f$, one obtains $H \leq 0$ corresponding to an “athermal” ($H = 0$) or a self-cooling ($H < 0$) laser. The condition for a laser to operate at a radiation balance regime is:

$$\frac{i_P^{\min}}{i_P} + \frac{i_L^{\min}}{i_L} = 1. \quad (3)$$

Here the minimum pump i_P^{\min} and minimum intra-cavity laser intensities i_L^{\min} for achieving the radiation balance are defined by

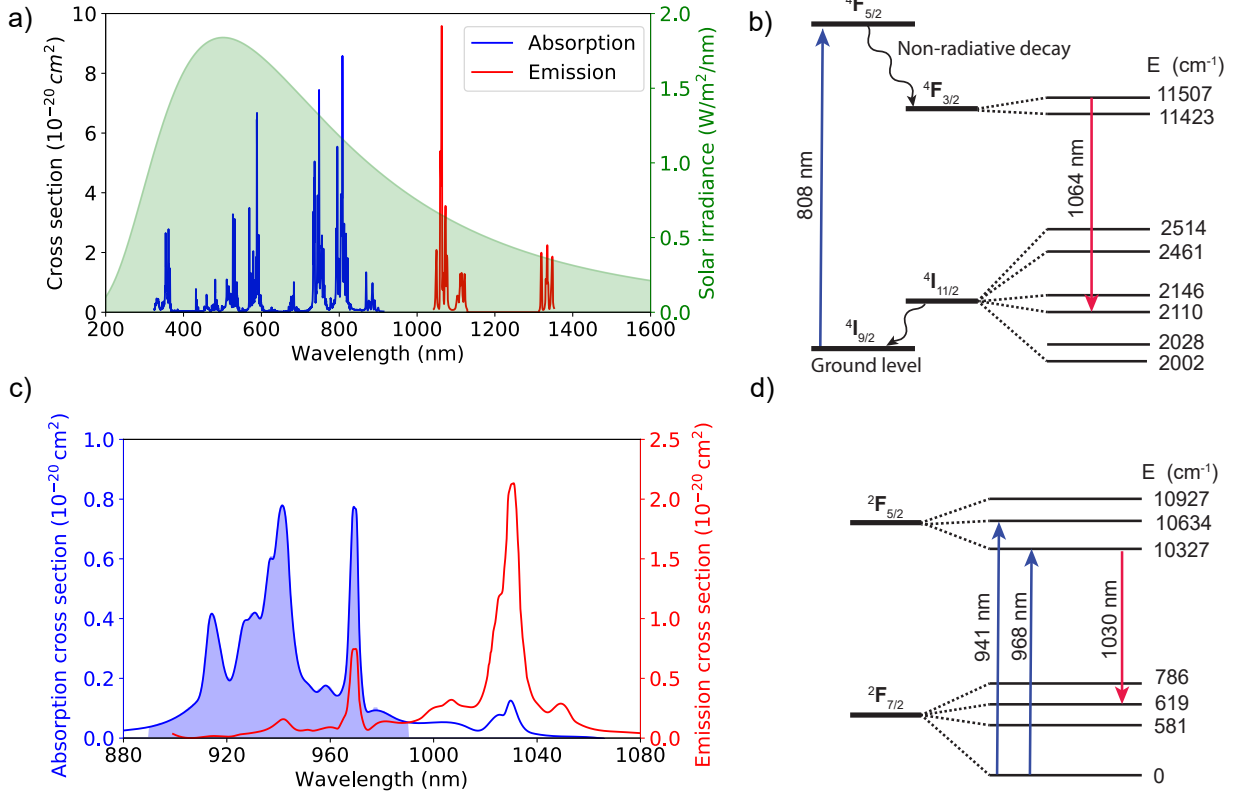


FIG. 6: **Lasing properties of Nd³⁺ and Yb³⁺ ions.** a) Absorption and emission cross sections of Nd³⁺ overlaid with extraterrestrial solar irradiance. b) Energy level diagram of the Nd:YAG gain medium. c) Absorption and emission cross-section of Yb³⁺. The blue shaded area shows the spectral bandwidth of the absorption cross section of Yb³⁺, which is filtered in the solar spectrum to pump the Yb³⁺ gain medium. d) Energy level diagram of the Yb:YAG gain medium.

$$i_P^{\min} = \frac{\beta_L}{\beta_P - \beta_L} \frac{\nu_C - \nu_L}{\nu_P - \nu_L}, \quad i_L^{\min} = \frac{\beta_P}{\beta_P - \beta_L} \frac{\nu_C - \nu_P}{\nu_P - \nu_L}, \quad (4)$$

where the fractional excitation required to bleach the transition at λ_i relative to its absorption σ_{abs} and emission σ_{ems} cross section is defined as:

$$\beta_i = \frac{\sigma_{\text{abs}}(\lambda_i)}{\sigma_{\text{abs}}(\lambda_i) + \sigma_{\text{ems}}(\lambda_i)}, \quad \beta_{PL} = \frac{\beta_P \beta_L}{\beta_P - \beta_L}, \quad (5)$$

and ν_C is defined as the zero crossing frequency.

Saturation intensities are defined as

$$I_{P\text{sat}} \equiv \frac{h\nu_P}{\tau_F(\sigma_{\text{abs}}(\lambda_P) + \sigma_{\text{ems}}(\lambda_P))}, \quad I_{L\text{sat}} \equiv \frac{h\nu_L}{\tau_F(\sigma_{\text{abs}}(\lambda_L) + \sigma_{\text{ems}}(\lambda_L))}, \quad (6)$$

where τ_F is the fluorescence lifetime.

The optimum value for intra-cavity lasing intensity is defined as⁴⁶:

$$i_L = (i_P + 1) \left(\sqrt{\frac{1}{\xi} \cdot \frac{i_P \left(\frac{\beta_P}{\beta_L} - 1 \right) - 1}{i_P + 1}} - 1 \right). \quad (7)$$

DECLARATIONS

This work was supported by research funding from the Max Planck Society. The authors do not declare any competing interests. The data supporting this study's findings are available from the corresponding author upon reasonable request.

REFERENCES

¹M. Küblböck, J. Will, and H. Fattah, *APL Photonics* **9** (2024).

²NATIONAL SECURITY SPACE OFFICE (NSSO) WASHINGTON DC, “Space-based solar power as an opportunity for strategic security: Phase 0 architecture feasibility study,” (2007).

³C. Algara, I. García, M. Delgado, R. Peña, C. Vázquez, M. Hinojosa, and I. Rey-Stolle, *Joule* **6**, 340 (2022).

⁴H. Hemmati, *Opt. Photon. News* **18**, 22 (2007).

⁵O. Edenhofer, R. Pichs-Madruga, Y. Sokona, K. Seyboth, S. Kadner, T. Zwickel, P. Eickemeier, G. Hansen, S. Schlömer, C. von Stechow, *et al.*, *Renewable energy sources and climate change mitigation: Special report of the intergovernmental panel on climate change* (Cambridge University Press, 2011).

⁶D. J. MacKay, *Sustainable Energy-without the hot air* (Bloomsbury Publishing, 2016).

⁷N. Brandon, F. Armstrong, S. Chan, B. David, R. Dittmeyer, J. Durant, A. Guwy, K. Hirose, A. Kucernak, I. Metcalf, *et al.*, *Climate Change: Science and Solutions, Briefing* **4**, 1 (2021).

⁸A. I. Osman, N. Mehta, A. M. Elgarahy, M. Hefny, A. Al-Hinai, A. H. Al-Muhtaseb, and D. W. Rooney, *Environmental Chemistry Letters* **20**, 153 (2022).

⁹C. Young, *Applied optics* **5**, 993 (1966).

¹⁰D. Garcia, D. Liang, C. R. Vistas, H. Costa, M. Catela, B. D. Tibúrcio, and J. Almeida, *Energies* **15**, 5292 (2022).

¹¹B. do Couto and D. Liang, in *International Conference on Applications of Optics and Photonics*, Vol. 8001 (SPIE, 2011) pp. 1135–1140.

¹²D. Liang and J. Almeida, *Applied optics* **51**, 6382 (2012).

¹³H. Danielmeyer, M. Blätte, and P. Balmer, *Applied physics* **1**, 269 (1973).

¹⁴L. D. Merkle, M. Dubinskii, K. L. Schepler, and S. M. Hegde, *Opt. Express* **14**, 3893 (2006).

¹⁵J. Foster and L. Osterink, *Journal of Applied Physics* **41**, 3656 (1970).

¹⁶D. H. Stone and M. D. Rotondaro, *Appl. Opt.* **31**, 1314 (1992).

¹⁷H. J. Eichler, A. Haase, R. Menzel, and A. Siemoneit, *Journal of Physics D: Applied Physics* **26**, 1884 (1993).

¹⁸W. Koechner, *Appl. Opt.* **9**, 2548 (1970).

¹⁹Z. Guan, C. Zhao, J. Li, D. He, and H. Zhang, *Optics & Laser Technology* **107**, 158 (2018).

²⁰S. Berwal, N. Khatri, and D. Kim, *Applied Surface Science Advances* **12**, 100348 (2022).

²¹K. M. Sh. Payziyev and F. Shayimov, *Uzbekiston Fizika Zhurnali* **21** (2019).

²²P. Yang, P. Deng, and Z. Yin, *Journal of luminescence* **97**, 51 (2002).

²³H. Fattahi, H. G. Barros, M. Gorjan, T. Nubbemeyer, B. Alsaif, C. Y. Teisset, M. Schultze, S. Prinz, M. Haefner, M. Ueffing, *et al.*, *Optica* **1**, 45 (2014).

²⁴E. Snitzer, *Journal of Applied Physics* **32**, 36 (1961).

²⁵W. S. Martin and J. P. Chernoch, “Multiple internal reflection face-pumped laser,” (1972), uS Patent 3,633,126.

²⁶J. Eggleston, L. Frantz, and H. Injeyan, *IEEE journal of quantum electronics* **25**, 1855 (1989).

²⁷A. Giesen, H. Hügel, A. Voss, K. Wittig, U. Brauch, and H. Opower, *Applied Physics B* **58**, 365 (1994).

²⁸T. Nubbemeyer, M. Kaumanns, M. Ueffing, M. Gorjan, A. Alismail, H. Fattahi, J. Brons, O. Pronin, H. G. Barros, Z. Major, *et al.*, *Optics letters* **42**, 1381 (2017).

²⁹H. Fattahi, A. Alismail, H. Wang, J. Brons, O. Pronin, T. Buberl, L. Vámos, G. Arisholm, A. M. Azzeer, and F. Krausz, *Optics letters* **41**, 1126 (2016).

³⁰A. Li, M. Bahri, R. M. Gray, S. Choi, S. Hoseinkhani, A. Srivastava, A. Marandi, and H. Fattahi, *APL Photonics* **9** (2024).

³¹M. Endo, *Optics express* **15**, 5482 (2007).

³²B. Wang, L. Lan, Y. Liu, Y. Tang, and Y. Zhang, *Journal of Russian Laser Research* **44**, 682 (2023).

³³K. Petermann, D. Fagundes-Peters, J. Johannsen, M. Mond, V. Peters, J. Romero, S. Kutowoi, J. Speiser, and A. Giesen, *Journal of crystal growth* **275**, 135 (2005).

³⁴A. Giesen and J. Speiser, *IEEE Journal of Selected Topics in Quantum Electronics* **13**, 598 (2007).

³⁵G. Nemova, *Applied Sciences* **11**, 7539 (2021).

³⁶S. R. Bowman, S. P. O'Connor, S. Biswal, N. J. Condon, and A. Rosenberg, *IEEE Journal of Quantum Electronics* **46**, 1076 (2010).

³⁷S. Bowman, *IEEE Journal of Quantum Electronics* **35**, 115 (1999).

³⁸S. Bowman, N. Jenking, S. O'Connor, and B. Feldman, *IEEE Journal of Quantum Electronics* **38**, 1339 (2002).

³⁹S. R. Bowman, *IEEE journal of quantum electronics* **35**, 115 (1999).

⁴⁰C. E. Mungan, *JOSA B* **20**, 1075 (2003).

⁴¹Y. Lei, B. Zhong, X. Duan, C. Wang, J. Xu, Z. Zhang, J. Ding, and J. Yin, *Frontiers of Physics* **18**, 42300 (2023).

⁴²R. I. Epstein and M. Sheik-Bahae, *Optical Refrigeration: Science and Applications of Laser Cooling of Solids* (2009).

⁴³G. Nemova, *Applied Sciences* **11**, 7539 (2021).

⁴⁴G. Nemova and R. Kashyap, *Optics Communications* **319**, 100 (2014).

⁴⁵Z. Yang, J. Meng, A. R. Albrecht, and M. Sheik-Bahae, *Optics express* **27**, 1392 (2019).

⁴⁶M. Sheik-Bahae and Z. Yang, *IEEE Journal of Quantum Electronics* **56**, 1 (2020).

⁴⁷R. I. Epstein and M. Sheik-Bahae, in *Optical Refrigeration: Science and Applications of Laser Cooling of Solids* (Wiley-VCH, 2009) pp. 1–32.

⁴⁸S. Ghonge, M. Kuno, and B. Janko, *APL Photonics* **9**, 081301 (2024).

⁴⁹E. Kanchanavaleerat, D. Cochet-Muchy, M. Kokta, J. Stone-Sundberg, P. Sarkies, J. Sarkies, and J. Sarkies, *Optical Materials* **26**, 337 (2004).

⁵⁰Crylaser Inc, “Datasheet,” (2023).

⁵¹H. Qiu, P. Yang, J. Dong, P. Deng, J. Xu, and W. Chen, *Materials Letters* **55**, 1 (2002).

⁵²X. Yan, J. Zheng, X. Jiang, M. Li, M. Li, and Z. Wang, *Laser Physics Letters* **11**, 125002 (2014).

⁵³H. Mashaal, Y. Eliezer, and A. Bahabad, *Optics Letters* **37**, 3516 (2012).

⁵⁴A. Agarwal and G. Gbur, *Journal of Optics* **17**, 103501 (2015).

⁵⁵D. C. Brown and V. A. Vitali, *IEEE Journal of Quantum Electronics* **47**, 3 (2011).

⁵⁶M. Wu, Y. Zeng, G. Zhu, Z. He, X. Ma, and X. Zhu, *Optics Letters* **48**, 4488 (2023).

⁵⁷M. Wohlmuth, C. Pflaum, K. Altmann, M. Paster, and C. Hahn, *Opt. Express* **17**, 17303 (2009).

⁵⁸M. Wohlmuth, K. Altmann, J. Werner, and C. Pflaum, in *Solid State Lasers XIX: Technology and Devices*, Vol. 7578 (SPIE, 2010) pp. 616–627.

⁵⁹W. Fan, Y. Liu, P. Guo, R. Deng, N. Li, F. Ding, Y. Li, J. Zhou, and S. Xie, *Current Optics and Photonics* **4**, 50 (2020).

⁶⁰L. Wang, Z. Yuan, Y. Zhao, and Z. Guo, *Journal of Thermal Science* **28**, 929 (2019).

⁶¹J. Speiser, in *Laser Sources and Applications III*, Vol. 9893 (SPIE, 2016) pp. 87–97.